AGU PUBLICATIONS

JGR

Journal of Geophysical Research: Oceans

RESEARCH ARTICLE

10.1002/2015JC011000

Key Points:
- An upwelling off the northeastern coast of Hainan Island (HNEU) was observed in summer 2009
- The HNEU is mainly intensified by along-isobath barotropic pressure gradient force
- Baroclinic processes make negative contributions to the HNEU

Correspondence to:
J. Hu,
hujy@xmu.edu.cn

Citation:
Lin, P., P. Cheng, J. Gan, and J. Hu (2016), Dynamics of wind-driven upwelling off the northeastern coast of Hainan Island, *J. Geophys. Res. Oceans*, *121*, doi:10.1002/2015JC011000.

Received 23 MAY 2015
Accepted 13 JAN 2016
Accepted article online 19 JAN 2016

Dynamics of wind-driven upwelling off the northeastern coast of Hainan Island

Peigen Lin[1], Peng Cheng[1], Jianping Gan[2], and Jianyu Hu[1]

[1]State Key Laboratory of Marine Environmental Science, College of Ocean and Earth Sciences, Xiamen University, Xiamen, Fujian, China, [2]Division of Environment and Department of Mathematics, Hong Kong University of Science and Technology, Hong Kong, China

Abstract Both observational and reanalysis sea surface temperature data reveal that upwelling occurs frequently off the northeastern coast of Hainan Island (downstream of the change in topography off Tongluo Cape), which cannot be attributed to the along-shelf wind alone. To identify dynamics of the upwelling, we conduct a numerical experiment using an idealized topography that is simplified from the actual topography off the eastern and northeastern coasts of Hainan Island. The result indicates that the upwelling downstream of the change in topography is associated with onshore cross-isobath transport. Analysis of the vertically integrated momentum balance shows that the upwelling-linked onshore transport is primarily intensified by the along-isobath barotropic pressure gradient force (PGT), but is weakened by the along-isobath baroclinic pressure gradient force (PGC). The along-isobath PGT is linked to the advection of relative vorticity, the bottom stress curl and the gradient of momentum flux in vorticity equation. On the other hand, the PGC-related process is diagnosed by potential vorticity (PV) balance. Similar to the negative PV term from wind stress, the negative PV terms of the joint effect of baroclinicity and relief and the baroclinic bottom pressure torque weaken the upwelling-linked onshore transport downstream of the change in topography. The onshore transport is enhanced by the positive PV from bottom stress. In addition, the cross-isobath forces play an important role in upwelling intensification in the shallow nearshore region.

1. Introduction

Upwelling prevails in the northern South China Sea (SCS) during summer [*Guan and Chen*, 1964; *Wu and Li*, 2003]. The upwelling off the northeastern coast of Hainan Island (or the Hainan northeastern upwelling; HNEU) is normally centered north of the Tongluo Cape (the schematic extent noted by red circle in Figure 1). The HNEU has been discussed generally in the Qiongdong upwelling system [see *Xie et al*., 2012 for a review], which is one of the most important topics of oceanographic studies in the SCS. Wind-driven Ekman transport along the east coast of Hainan Island is believed to drive the upwelling system [*Han et al*., 1990], with mean delay time of 2.2 days [*Jing et al*., 2015]. Ekman pumping induced by the wind stress curl also contributes to the generation of the upwelling [*Jing et al*., 2009]. Using a high-resolution three-dimensional hydrodynamic model, *Su and Pohlmann* [2009] indicated that along-shelf topographic variation affects the location of the upwelling center and noted that the vertical mixing due to the internal wave is important for the upwelling. In addition, fresh water from rivers tends to inhibit the upwelling outcropping to surface in the nearshore area [*Gan et al*., 2009b; *Su et al*., 2011].

A few studies have analyzed the HNEU specifically. *Yu* [1987] pointed out that the HNEU might be an eddy-driven upwelling that is intensified by southwesterly wind in the summer. *Li* [1990] speculated that the northeastward current, affected by the bottom topography and the changing coastline, causes a vertical circulation and induces the HNEU. This was later confirmed by *Li et al*. [2012] using the Princeton Ocean Model. They showed that the enhanced large-scale circulation flows along the east coast of Hainan Island and turns toward the northeast shelf, subsequently, intensifying the HNEU; and the bottom topography is important in this process. In addition to wind, eddies and currents, tides are also important drivers in the HNEU area [*Song et al*., 2012].

Previous studies have revealed the existence of the HNEU and have described its basic characteristics, but the dynamics of the HNEU, particularly the roles of topography and baroclinic effects, remain

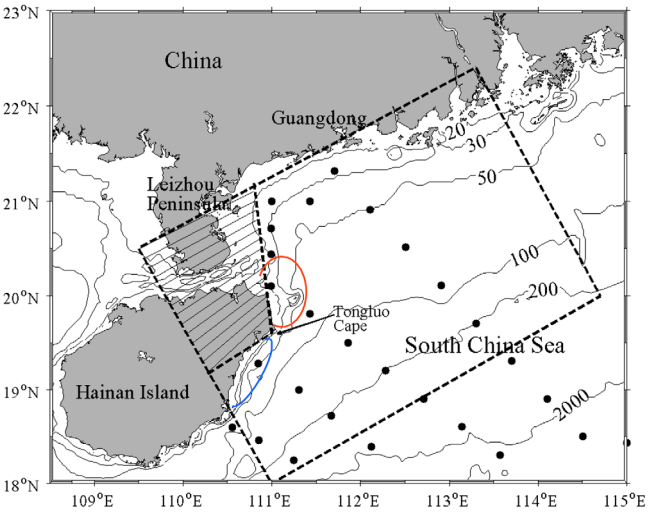

Figure 1. Sampling stations (dots) off the eastern and northeastern coasts of Hainan Island for the cruise in summer 2009. The red and blue circles note the schematic locations of the upwellings off northeastern and eastern coasts of Hainan Island, respectively. The geography of the area in the dashed box is idealized for the model simulation. Bathymetric contours are in meters.

unclear. The shelf off the eastern coast of Hainan Island is steep and widens substantially to the northeast from the shelf off Tongluo Cape (Figure 1). Accordingly, the southwest-northeast coastline and isobaths turn their orientation to south-north. This special topography plays an important role in the generation of coastal upwelling. Under upwelling-favorable wind forcing, coastal upwelling is intensified to a greater extent over a narrow shelf with a steep slope than over a wide shelf with a gentle slope [*Gan et al*., 2009a; *Gu et al*., 2012; *Chen et al*., 2013]. The alongshore-varying topography controls the location and intensity of coastal upwelling [*Song et al*., 2001; *Gan and Allen*, 2002]. Particularly, coastal upwelling intensifies at the downstream of a cape [*Barth et al*., 2000] and a canyon [*Allen*, 1996]. *Pringle* [2002] analyzed the linear barotropic potential vorticity (PV) balance and suggested that upwelling-linked onshore transport forced by wind is intensified in the bottom boundary layer where the shelf narrows downwind. This topography-induced cross-shore transport has been found to largely link with an along-isobath pressure gradient force [*Gan et al*., 2009a]. *Weisberg et al*. [2001] suggested that bottom pressure torque, the curl of vertically integrated pressure gradient force, balances the relative vorticity over the shelf break and the bottom stress torque over the inner shelf in situations where the surface and bottom boundary layers are dynamically important. In barotropic PV balance, the along-isobath pressure gradient force was found to be induced by the net stress curl in the water column over a shelf with weak stratification [*Gan et al*., 2013], and by advection of vorticity as well off a coastal cape and over a submerged valley [*Liu and Gan*, 2014, 2015].

It is also worthwhile to identify the effect of density field on upwelling. Stratification may reinforce the wind-driven cross-shelf circulation and then upwelling [*Weisberg et al*., 2000]. The wind-driven surface offshore transport is offset by the return flow in bottom layer under weak stratification (Burger number $S \ll 1$) and in the interior layer under strong stratification ($S \geq 1$) [*Lentz and Chapman*, 2004]. The cross-shelf circulation tends to be reduced and the wind-driven upwelling can be confined at nearshore region in stratified condition [*Lentz*, 2001; *Austin and Lentz*, 2002]. *Gan et al*. [2009b] suggested that horizontal density gradient, generating along-isobath baroclinic pressure gradient force, modifies the alongshore distribution of cross-isobath transport under wind forcing. The baroclinic effect is manifested primarily through the joint effect of baroclinicity and relief (JEBAR) term [*Gan et al*., 2013].

In addition, cross-shelf circulation is generally linked to along-shelf momentum but is rarely attributed to cross-shelf forcing terms (cross-shelf wind stress and pressure gradient force). *Horwitz and Lentz* [2014] derived an empirical relationship between the cross-shelf density gradient and cross-shelf transport. Generally, the cross-shelf wind stress is more significant than the along-shelf wind stress in driving the cross-shelf circulation over an inner continental shelf [*Tilburg*, 2003; *Fewings et al*., 2008].

Developing a realistic numerical model to simulate the HNEU could help explain the dynamics of the HNEU, but it would still be difficult to explore the contribution of a particular process. This study, therefore, conducted process-oriented idealized numerical experiments that are configured based on the basic characteristics of the HNEU and explored the dynamic processes. Of most interest are the effects of flow-topography interaction, baroclinic dynamics, and cross-isobath forces on the HNEU.

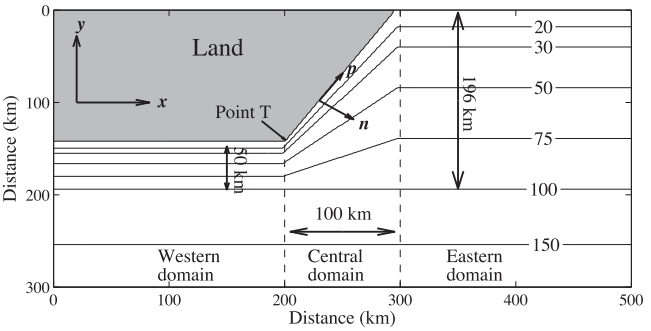

Figure 2. Domain of the idealized numerical model. The coordinate system (*p, n*) is a rotation from (*x, y*) where the coordinate *p* is parallel to the isobaths and the coordinate *n* is normal to the isobaths. Contours denote water depth in meters.

2. Materials and Methods

2.1. Hydrographic Observations

A cruise covering 81 sampling stations was conducted in the northern SCS from 16 July to 15 August 2009. The bottom topography of the study area and the observation stations are shown in Figure 1. Temperature and salinity data were obtained using Seabird SBE 911 and 917 conductivity, temperature, and depth (CTD) profilers.

2.2. Reanalysis Data

The daily, high-resolution (1/20° ×1/20°) sea surface temperature (SST) data produced by the Operational SST and Sea Ice Analysis (OSTIA) system (http://ghrsst-pp.metoffice.com/pages/latest_analysis/ostia.html) are used to generate a weekly averaged data set for the summers (June, July and August) of 2006–2012. The daily blended wind data with a resolution of 0.25° for the same time period are produced by the National Climatic Data Center (NCDC; https://www.ncdc.noaa.gov/oa/rsad/air-sea/seawinds.html). We calculated the weekly wind data to match the timescale of the SST images.

The fuzzy *c*-means (FCM) algorithm, a pixel classification method that has been successfully applied in upwelling studies [e.g., *Sousa et al*., 2008; *Chen et al*., 2012], is used to identify upwelling regions from weekly SST images. The FCM classifies pixels in each image into *c* fuzzy clusters based on the iterative approximation from initial clusters.

2.3. Numerical Experiment

The Regional Ocean Modeling System (ROMS), which is a free-surface, hydrostatic, primitive equations ocean model [*Shchepetkin and McWilliams*, 2005], is used to examine the dynamics of the HNEU. The model domain (Figure 2), with dimensions of 500 km × 300 km, is an idealized geography of regions off the coasts of eastern Hainan Island and southern Guangdong (Figure 1, dashed box). The land located northwest of the model domain represents the Hainan Island and the Leizhou Peninsula. The western domain ($x < 200$ km) with a 50 km wide continental shelf (depth < 100 m) refers to the shelf off the eastern coast of Hainan Island, while the eastern domain ($x > 300$ km) with a 196 km wide shelf is simplified from the shelf off the coast of Guangdong. The central domain (between $x = 200$ km and $x = 300$ km) represents the shelf off the northeastern coast of Hainan Island. Accordingly, the change in topography off Tongluo Cape is at $x = 200$ km in the model domain. The water depth increases from 10 m off the northern coast to 200 m at the southern boundary. A radiation boundary condition is imposed on the southern boundary. Following *Gan et al*. [2005], a periodic boundary condition is chosen for the eastern and western boundaries. To apply this periodic boundary condition properly, an extended computational domain (not shown) is added next to the existing eastern boundary. This extended domain is west-east symmetric with the domain shown in Figure 2. Specifically, the eastward-extended domain also has dimensions of 500 km × 300 km with a land to the northeast, so the topography conditions on the eastern and western boundaries are matched.

The model grid has 2 km horizontal resolution and 30 vertical levels. It is initialized with a horizontally uniform density profile ($N^2 = 4.65 \times 10^{-4}$ s^{-2}) that is spatially averaged from all in situ data during the cruise in 2009. The initial velocity and surface elevation are set to zero. The model is forced by a spatially uniform westerly wind (5 m s^{-1}) that is representative of the mean southwesterly monsoon in the region during summer. The Mellor-Yamada 2.5 turbulence closure scheme [*Mellor and Yamada*, 1982] is applied to calculate vertical mixing. The model is run for 15 days, and the result on Day 8 when first reaching a quasi steady state, is used for analyses.

3. Results

3.1. Spatial Distribution of the Upwelling

A low-temperature and high-salinity core with a temperature of approximately 26.5°C and a salinity of 33.6 psu was located off the northeastern coast of Hainan Island at a depth of 3 m (Figures 3a and 3c). The

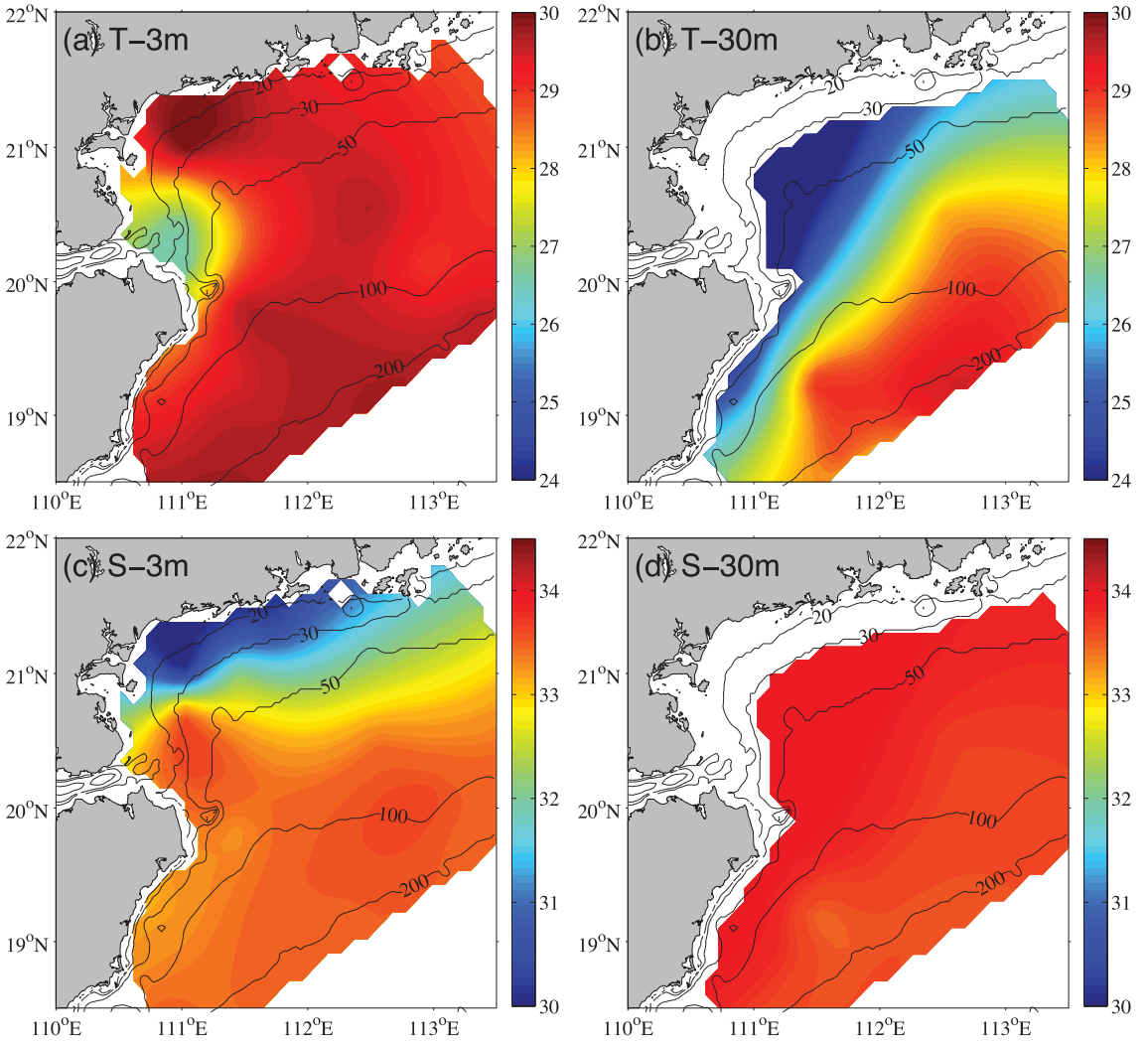

Figure 3. Distributions of temperature (top) and salinity (bottom) at depths of 3 m (a and c) and 30 m (b and d) during the cruise in summer 2009.

extent of cold and salty water at the 30 m depth covered the shelves off the eastern and northeastern coasts of Hainan Island (Figures 3b and 3d). The nearshore temperature was about 3°C lower than the temperature in the offshore region, and the salinity exceeded 34 psu in the nearshore region.

Figure 4b shows the result of the FCM algorithm with $c = 4$ clusters applied to the weekly SST image for the period 20–26 July 2009 (Figure 4a). The upwelling region is represented by cluster $c1$ (blue) in the FCM image, corresponding to the relatively cooler water in the SST image; this matches the hydrographic observations (Figure 3a) well.

The correlation coefficients (significance level >95%) between the time series of each SST pixel and the area-averaged weekly wind components in different directions (0°–90°, rotating clockwise from northward) were calculated for the study area (110°–113.5°E, 18.5°–22°N). Figure 5a shows that the maximum (black line) and the mean (gray line) correlations increase as the angle of wind component direction increases and are maximized at 25° and 35°, respectively. As such, we chose the time series of the wind component at 30° for the correlation analysis with the SST pixels.

Based on all the FCM images, the probability of upwelling occurrence is defined as the ratio of the number of upwelling events to the total number of SST images. The contours of upwelling probability show a banded structure near the eastern and northeastern coasts of Hainan Island (Figure 5b). The locations of

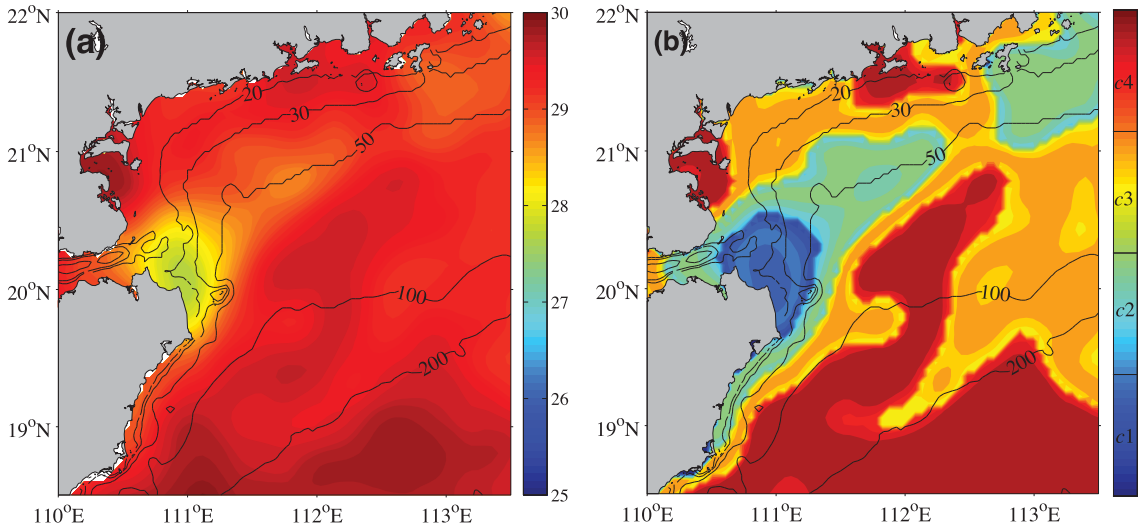

Figure 4. (a) Weekly OSTIA SST (°C) image for the period 20–26 July 2009; and (b) the corresponding FCM 4-partition image with the upwelling area colored in blue.

the two cores with relatively high probabilities (>60%) indicate that the upwelling presents most frequently off the northeastern and eastern coasts of Hainan Island, respectively. The former refers general extent of the HNEU, which we focus on in this study.

The correlation coefficients between the time series of wind stress component in the 30° direction and the time series of the SST at each pixel from 2006 to 2012 are negative in the domain (Figure 5b). The high-correlation band (correlation coefficient < -0.4) has two branches: one extends along the contour of upwelling probability toward the northeastern coast of Hainan Island, which implies that the upwelling in this region is correlated with the southwesterly wind; the other extends to the east along the 75 m isobath (see details in section 4).

3.2. Model Results

3.2.1. Upwelling Characteristics and Cross-Isobath Transport

For convenience, the change in topography at $x = 200$ km in the model domain will be represented as "Point T." The direction of current nearshore will be referred to as the "downstream" direction.

In Figure 6a, the temperature at a depth of 3 m is apparently low along the coast in the western and central domains. Under the upwelling-favorable wind, the nearshore currents are spun up and flow along the coastline with an eastward branch that appears offshore around Point T (Figure 6b). The onshore depth-integrated velocity reaches its maximum downstream of Point T along the 60 m isobath. It suggests that the upwelling is linked to the onshore cross-isobath transport, which can be intensified by the particular topography.

To study the horizontal and vertical variations of the cross-isobath transport associated with the upwelling, we transformed the momentum equations to a rotating coordinate system in which p indicates the along-isobath direction and n indicates the normal direction of isobaths (Figure 2). Under stratified conditions, the baroclinic processes driven by the density field have significant effects on the upwelling. Hence, the pressure gradient force terms are decomposed into the baroclinic and barotropic pressure gradient forces. The along-isobath vertically integrated momentum balance [*Huthnance*, 1984] is:

$$\overbrace{\frac{\partial}{\partial t}\int_{-h_2}^{-h_1} v^p dz}^{\text{ACC}} + \overbrace{\frac{\partial}{\partial n}\int_{-h_2}^{-h_1} u^n v^p dz + \frac{\partial}{\partial p}\int_{-h_2}^{-h_1} v^p v^p dz}^{\text{GMF}} + \overbrace{f\int_{-h_2}^{-h_1} u^n dz}^{\text{Coriolis force}} = \overbrace{-\frac{\partial \chi}{\partial p} - \frac{g}{\rho_0}\left(\frac{\partial h_1}{\partial p}\int_{-h_1}^{0}\rho dz' - \frac{\partial h_2}{\partial p}\int_{-h_2}^{0}\rho dz'\right)}^{\text{PGC}} + \overbrace{\int_{-h_2}^{-h_1}\left(-g\frac{\partial \zeta}{\partial p} + K_h\nabla^2 v^p + \frac{\tau^p}{\rho_0}\right)dz}^{\text{PGT+HVI+VVI}}, \quad (1)$$

and the cross isobath vertically integrated momentum balance is

$$\frac{\partial}{\partial t}\int_{-h_2}^{-h_1} u^n dz+\frac{\partial}{\partial n}\int_{-h_2}^{-h_1} u^n u^n dz+\frac{\partial}{\partial p}\int_{-h_2}^{-h_1} u^n v^p dz-f\int_{-h_2}^{-h_1} v^p dz$$
$$=-\frac{\partial \chi}{\partial n}-\frac{g}{\rho_0}\left(\frac{\partial h_1}{\partial n}\int_{-h_1}^{0}\rho dz'-\frac{\partial h_2}{\partial n}\int_{-h_2}^{0}\rho dz'\right)+\int_{-h_2}^{-h_1}\left(-g\frac{\partial \zeta}{\partial n}+K_h\nabla^2 u^n+\frac{\tau^n}{\rho_0}\right)dz, \quad (2)$$

where

$$\chi=\frac{g}{\rho_0}\int_{-h_2}^{-h_1}\left(\int_{-z}^{0}\rho dz'\right)dz, \quad (3)$$

ζ is the surface elevation, the Coriolis parameter $f=10^{-4}$ s^{-1}, the reference density $\rho_0=1025$ kg m^{-3}, and the depth $-h_1$ ($-h_2$) is the upper (lower) limit of the vertical integral. $U^n=\int_{-h_2}^{-h_1} u^n dz$ and $V^p=\int_{-h_2}^{-h_1} v^p dz$ are the cross-isobath and along-isobath transports integrated from $-h_1$ to $-h_2$, respectively. The terms on the left-hand side of equation (1) are the along-isobath acceleration (ACC) of the along-isobath transport, the gradient of cross-isobath and along-isobath nonlinear momentum flux (GMF), and the Coriolis force. On the right-hand side, the baroclinic pressure gradient force (PGC) consists of three terms: the term with χ is related to JEBAR (analyzed in section 3.2.3), and the other two terms represent the interaction between bottom pressure gradient force and topography. The barotropic pressure gradient force (PGT; the fourth term) depends only on the water surface slope. The fifth term is the horizontal viscosity (HVI), followed by the vertical viscosity (VVI).

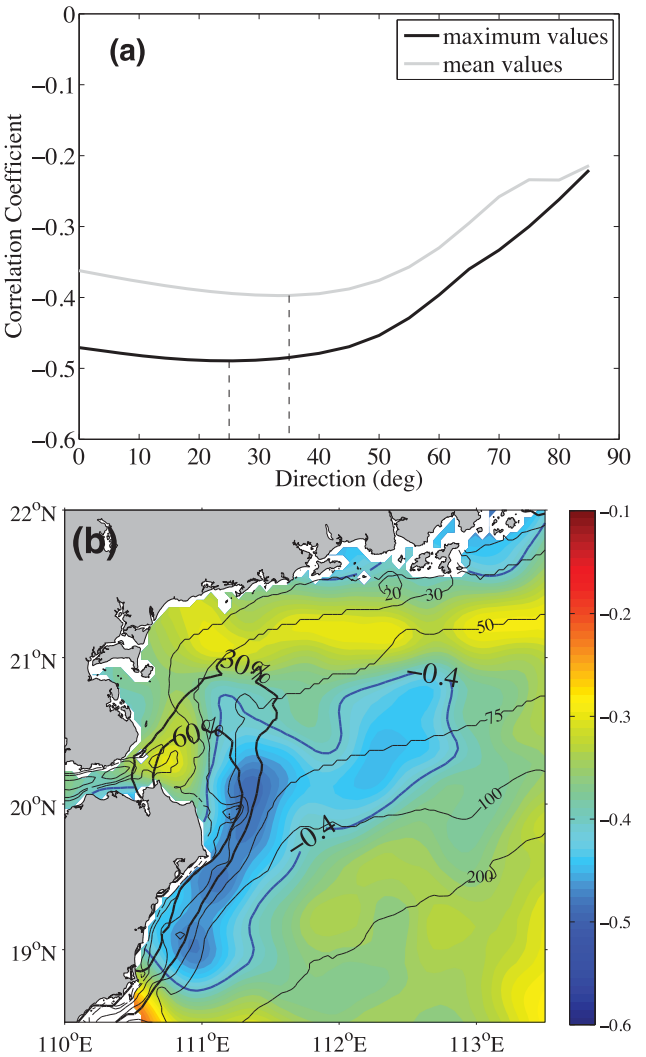

Figure 5. (a) Maximum and area-averaged correlation coefficients (significance level >95%) between the SST time series of each pixel and area-averaged estimates of different weekly wind stress components from 0° (northward) to 90° (eastward) for the summers of 2006–2012. (b) Spatial distribution of correlation coefficients between the wind stress component in the 30° direction and the SST at each pixel from 2006 to 2012. The −0.4 correlation coefficient contour (blue contour), and the 30% and 60% contours of upwelling probability (bold black contours) are highlighted, Bathymetric contours (thin black contours) are in meters.

To estimate U^n, in this analysis, we assumed that the water column has three layers: the surface layer, the interior layer, and the bottom layer [*Lentz and Chapman*, 2004]. The surface layer begins at the surface ($h_1=0$; the surface elevation is small in comparison with the water depth) and ends at the depth ($-h_2$) where the first zero velocity anomaly (obtained by subtracting the depth-averaged velocity) of the cross-isobath flow appeared. The layer from the second zero crossing of velocity anomaly ($-h_1$) to the bottom ($h_2=H$) is considered as the bottom layer [*Lentz*, 2001].

The cross-isobath velocity anomaly has a two-layer vertical structure along the 60 m isobath (the interface of these two layers is shown in Figure 9b). Based on equation (1), the driving factors of cross-isobath transports in the surface layer (U^S) and the bottom layer

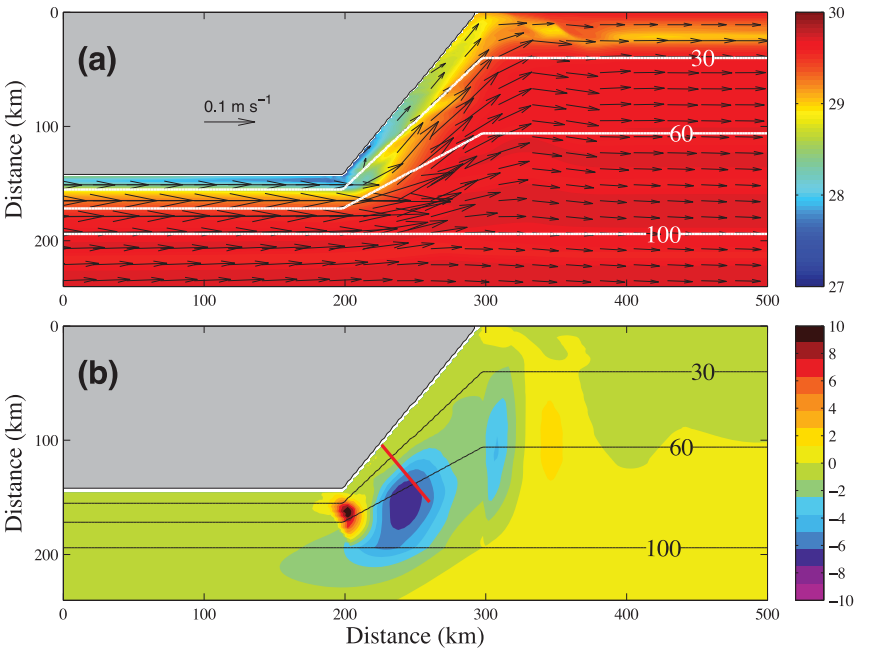

Figure 6. (a) Depth-averaged velocity vectors (m s^{-1}) superimposed on temperature (°C, color) at a depth of 3 m; (b) depth-integrated transport (m^2 s^{-1}) normal to the isobaths, with the positive (negative) values denoting offshore (onshore) direction as shown in Figure 2. The red line in Figure 6b denotes the section selected for analysis.

(U^B) along the 60 m isobath are shown in Figure 7. In the western domain, U^S (Figure 7a, dashed black line) is generated by the uniform offshore wind-driven transport which is expressed as the transport related to the vertical viscosity in the surface layer (Figure 7a, light blue line). The bottom stress (the vertical viscosity in the bottom layer) drives the onshore transport (Figure 7c, light blue line) to counteract U^S. It clearly suggests that the Ekman process is primary in the western domain.

The spatial variation in cross-isobath transport in the central domain is, however, very different. In the surface layer, the U^S is offshore around Point T and is onshore downstream. The maximum magnitudes of the offshore and onshore U^S are 4.8 m^2 s^{-1} and -2 m^2 s^{-1}, respectively. The pattern of PGT-induced transport (Figure. 7a, blue line) in the surface layer agreed with the U^S, suggesting that the cross-isobath transport in the surface layer is primarily geostrophic. The PGC-induced transport (Figure 7a, red line) is roughly zero downstream of Point T. The maximum cross-isobath nonlinear momentum flux term is balanced by the along-isobath nonlinear momentum flux term (Figure 7b). As a result, the total nonlinear momentum flux term is small but has a similar pattern to the PGT along the isobath.

The geostrophic transport induced by the pressure gradient force in the bottom layer has a similar spatial variation to that in the surface layer but has a larger magnitude. In particular downstream of Point T, the PGT-induced U^B is almost 3 times larger than the PGT-induced U^S. The U^B from the PGC shows a distribution opposite to that from the PGT, but these two components do not balance each other (Figure 7c). Although the bottom Ekman transport induced by vertical viscosity is small, it is an indispensable component in the dynamic process. Since the two nonlinear momentum flux terms balance each other (Figure 7d), the total nonlinear momentum flux term has the same sign as the PGT term but is 10 times smaller in magnitude. The contributions of the horizontal viscosity are small in both layers.

Here, the PGC only contains the χ-related term, because the other two terms are zero when the momentum equations are integrated throughout the entire water column (Figure 7e). The contributions of PGT and PGC to transport throughout the water column are similar to their contributions in surface and bottom layers, respectively. The transports induced by vertical viscosity in these two layers are balanced along the 60 m isobath except around Point T. The total nonlinear momentum flux term makes a positive contribution to the cross-isobath transport throughout the water column (Figure 7f).

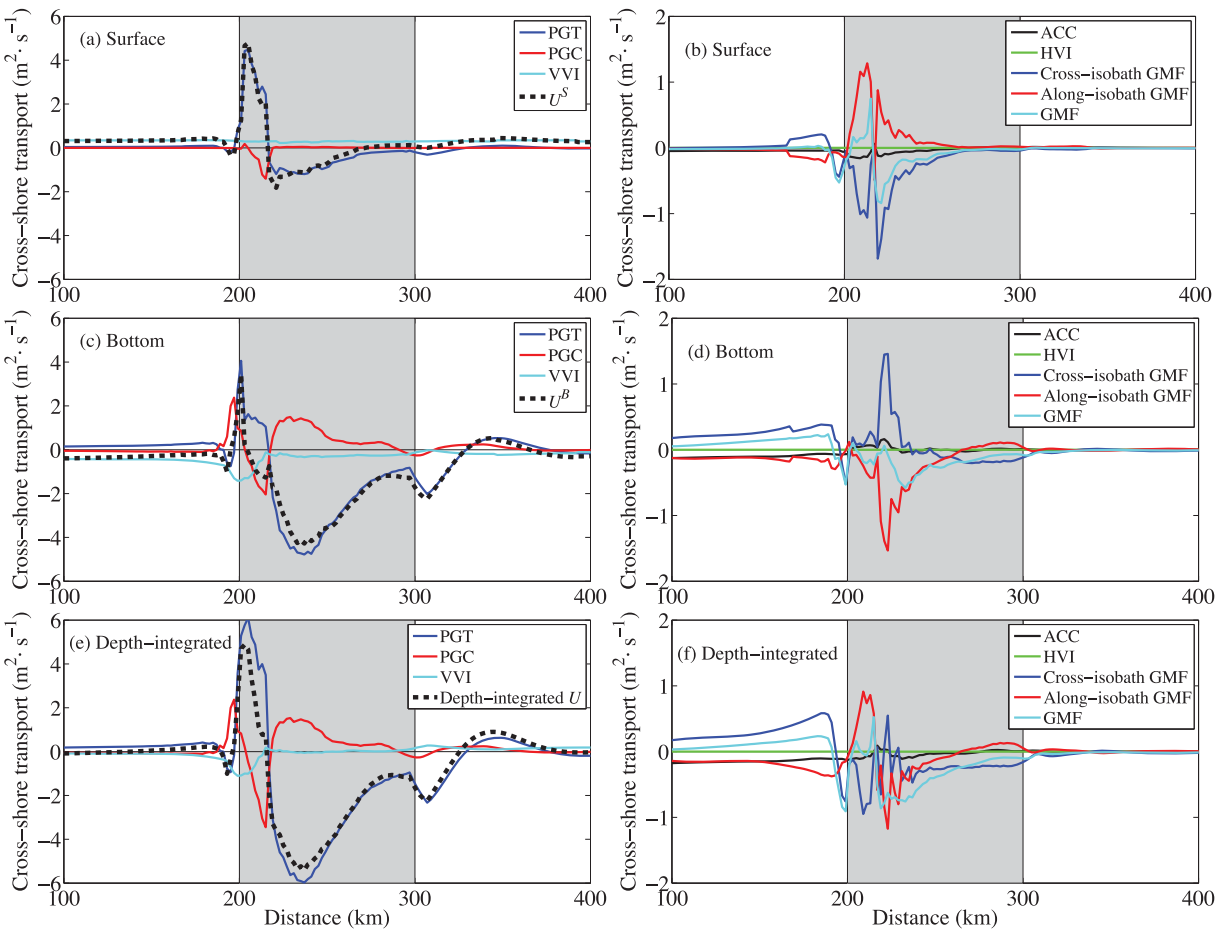

Figure 7. Cross-isobath transport ($m^2\ s^{-1}$) across the 60 m isobath attributable to terms of the along-isobath vertically integrated momentum equation, including (a, c, e) barotropic pressure gradient force (PGT, blue line), baroclinic pressure gradient force (PGC, red line), vertical viscosity (VVI, light blue line), and vertically-integrated transport (U^S or U^B, dashed black line) and (b, d, f) acceleration (ACC, black line), horizontal viscosity (HVI, green line), cross-isobath nonlinear momentum flux (GMF, blue line), along-isobath GMF (red line), and GMF (light blue line) in Figures 7a and 7b the surface layer, (Figures 7c, 7d) the bottom layer, and (Figures 7e, 7f) throughout water column. The positive (negative) values denote offshore (onshore) cross-isobath transport. The shaded area refers to the central domain.

The momentum balance analysis suggests that the along-isobath PGT is the primary driving factor for the intensified cross-isobath transport linked to the upwelling in the central domain, while the along-isobath PGC acts in the opposite way.

3.2.2. Barotropic Pressure Gradient Force

To assess the effect factors of the along-isobath PGT, we use the steady depth-integrated vorticity equation obtained from equations (1) and (2) with $h_1 = 0$ and $h_2 = H$ (for details see appendix of *Gan et al.* [2013]):

$$-g\frac{\partial \zeta}{\partial p}=\left(\frac{\partial H}{\partial n}\right)^{-1}\left[J\left(\psi,\bar{\xi}\right)+\frac{\partial H}{\partial n}\frac{\partial}{\partial p}\left(\frac{\bar{u}^2+\bar{v}^2}{2}\right)+\frac{\partial H}{\partial n}\frac{\partial}{\partial p}\int_{-H}^{0}\frac{\rho g}{\rho_0}dz\ -\nabla\times\left(\frac{\boldsymbol{\tau_s}}{\rho_0}\right)+\nabla\times\left(\frac{\boldsymbol{\tau_b}}{\rho_0}\right)-\nabla\times\int_{-H}^{0}(\mathrm{HVI})dz\right] \quad (4)$$

where H is the water depth, J is the Jacobian determinant, and ψ is the transport streamfunction defined by $U=-\partial\psi/\partial y$ and $V=\partial\psi/\partial x$. The depth-averaged relative vorticity is $\bar{\xi}=\partial\bar{v}/\partial x-\partial\bar{u}/\partial y$, where $\bar{u}$ and $\bar{v}$ are depth-averaged velocities. The wind stress and bottom stress are $\boldsymbol{\tau_s}$ and $\boldsymbol{\tau_b}=\boldsymbol{\tau}|_{-H}$. The bold symbols represent vectors. The first two terms on the right-hand side of equation (4), the advection of relative vorticity and the gradient of nonlinear momentum flux, are both derived from the nonlinear advection terms in the momentum equations. The third term is along-isobath bottom PGC. The fourth term is wind stress curl, which is zero because the model is forced by spatially uniform wind. The fifth term is bottom stress curl and the last term is horizontal viscous vorticity. The depth-integrated term with χ is zero after cross-differentiation, and the advection of planetary vorticity equals zero because the Coriolis parameter f is constant in this study.

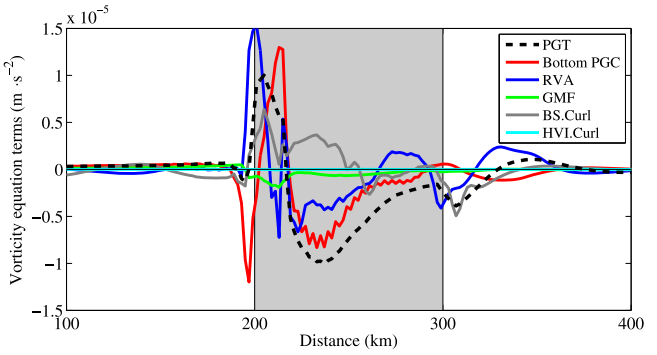

Figure 8. Along the 60 m isobath, terms ($m^2\ s^{-1}$) in the vorticity equation derived from depth-integrated momentum balances including PGT (dashed black line), PGC at bottom (red line), advection of relative vorticity (RVA, blue line), gradient of momentum flux (GMF, green line), bottom stress curl (BS.Curl, gray line), and horizontal viscous vorticity (HVI.Curl, light blue line). The shaded area refers to the central domain.

Each term in the vorticity equation (equation (4)) along the 60 m isobath is presented in Figure 8. The advection of relative vorticity (blue line) varies with the along-isobath PGT (dashed black line). The advection of relative vorticity is associated with the cyclonic or anticyclonic movement of current along the changing bottom topography. *Liu and Gan* [2014] pointed out that the bottom stress curl (gray line), which consists of the bottom curvature and the bottom shear vorticity, is another important term affecting the along-isobath PGT. Similarly, in our results, the bottom stress curl enhances the along-isobath PGT downstream of Point T. The gradient of nonlinear momentum flux (green line) is negative in the central domain owing to the decreasing along-isobath depth-averaged velocities. In other words, this term has a similar effect as the bottom stress curl on the along-isobath PGT. As a term originating from nonlinear advection terms in the momentum equations, nonlinear momentum flux is important in the region where the nonlinear process is significant. The small effect of horizontal viscous vorticity (light blue line), however, can be neglected.

The along-isobath bottom PGC (Figure 8, red line) displays a similar distribution to the along-isobath PGT. To reveal the spatial variation in the along-isobath PGT, we present the surface elevation along the 60 m isobath in Figure 9a. Generally, the surface elevation plunges around Point T and then gradually increases downstream in the central domain. Corresponding to this pattern of surface elevation, the along-isobath PGT enhances the onshore transport of denser water downstream of Point T (Figure 9b), and in turn, changes the along-isobath density gradient resulting in the along-isobath bottom PGC.

The advection of relative vorticity and the along-isobath PGT are nearly in-phase. The bottom stress curl is also a critical PGT-derived term downstream of Point T. Although its magnitude is small, the gradient of nonlinear momentum flux has a positive effect on the along-isobath PGT. As negative feedback, the along-isobath bottom PGC counteracts the along-isobath PGT.

3.2.3. Potential Vorticity Dynamics

Because the PGC is important for weakening the onshore transport and, in turn, the upwelling, we identified the baroclinic dynamics using the baroclinic PV balance without barotropic characteristics. The curl of the depth-averaged momentum equation [e.g., *Huthnance*, 1984; *Gan et al.*, 2013] is rewritten based on equations (1) and (2):

$$\frac{\partial \bar{\xi}}{\partial t} = -J\left(\bar{\psi}, \bar{\xi}\right) - J\left(\psi, \frac{f}{H}\right) + J\left(\chi, \frac{1}{H}\right) - \frac{gH}{\rho_0} J\left(\int_{-H}^{0} \rho dz, \frac{1}{H}\right) + \nabla \times \left(\frac{\tau_s}{H\rho_0}\right) - \nabla \times \left(\frac{\tau_b}{H\rho_0}\right), \tag{5}$$

where $\bar{\psi}$ is the streamfunction, $\bar{u} = -\partial\bar{\psi}/\partial y$ and $\bar{v} = \partial\bar{\psi}/\partial x$.

The left-hand side of equation (5) is the PV acceleration term referring to the temporal variation of PV. On the right-hand side, the first two terms are the

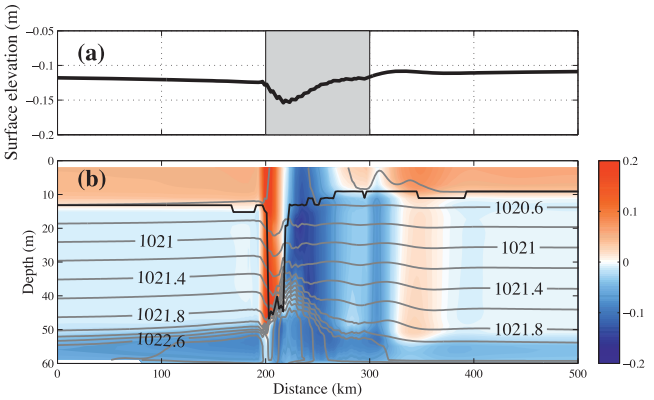

Figure 9. Along the 60 m isobath, (a) the distribution of surface elevation (m) and (b) the sectional distributions of cross-isobath velocity ($m\ s^{-1}$, color) with the interface between surface and bottom layers (black line) are shown and density contours are overlaid ($kg\ m^{-3}$). The shaded area in Figure 9a refers to the central domain. The positive (negative) values in Figure 9b denote offshore (onshore) cross-isobath velocity.

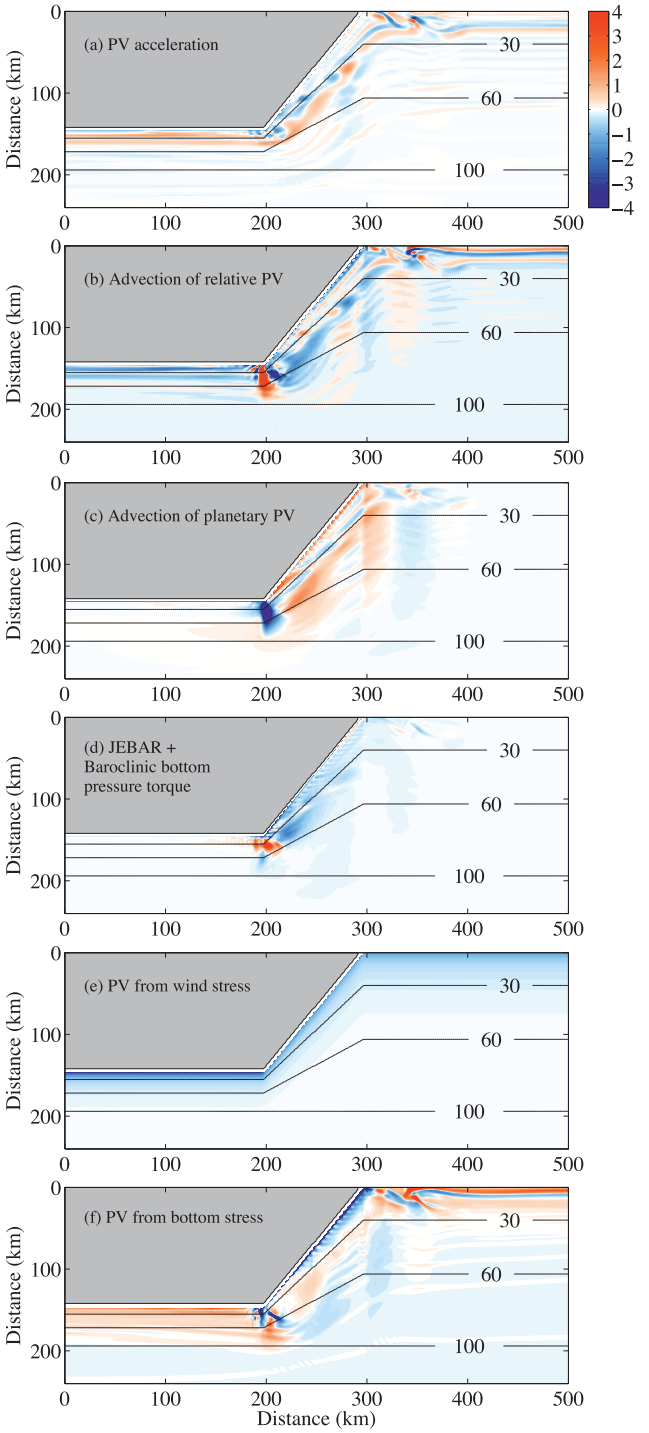

Figure 10. Spatial distribution of the terms ($\times 10^{-10}$ m^{-1} s^{-2}) in the potential vorticity equation (i.e., equation (6)) derived from depth-averaged momentum balances, including (a) PV acceleration, (b) advection of relative PV, (c) advection of planetary PV, (d) depth-averaged pressure torque (JEBAR + baroclinic bottom pressure torque), (e) PV from wind stress, and (f) PV from bottom stress.

advections of relative and planetary PV. The third term is the JEBAR term, and the fourth term is the baroclinic bottom pressure torque as related to the density field of the water column. The last two terms (the fifth and sixth) are the PV terms induced by wind stress and bottom stress, respectively. The HVI-induced PV is not taken into account owing to its small magnitude.

The PV acceleration is relatively small (Figure 10a). The advection of relative PV term (Figure 10b) is positive around Point T and is negative downstream. The positive and negative advections of relative PV are related to anticyclonic and cyclonic movements of coastal currents, respectively. The advection of relative PV is balanced by the advection of planetary PV (Figure 10c), which is only related to the bottom topography due to the constant f in this study. As noted by *Mertz and Wright* [1992], the depth-averaged pressure torque (Figure 10d) consists of the JEBAR term and the PV term associated with the bottom pressure torque. The latter, in this study, is negative over the onshore area of the central domain except in the region around Point T. However, JEBAR can be eliminated when the water column is homogeneous or when the bottom topography is flat [*Gan et al.*, 2013]. As the PV components associated with density field and topography, the baroclinic bottom pressure torque and the JEBAR have similar distributions (not shown). *Myers et al.* [1996] indicated that JEBAR is analogous to the PV from wind stress (Figure 10e). Therefore, downstream of Point T, the negative JEBAR and the baroclinic bottom pressure torque terms weaken the upwelling-linked onshore transport. The effect of JEBAR and baroclinic bottom pressure torque terms can also be explained with respect to momentum balance. After depth integration, the PGC term in equations (1) and (2) only remains the component involving χ (related to JEBAR term in PV equations). As shown in Figure 7e, the χ-related component of the PGC term weakens the onshore transport downstream of Point T. The effect of the baroclinic bottom pressure torque term on PV balance also lends further support to the results of the

vorticity analysis; that is, the baroclinic bottom pressure gradient force plays a negative role in the along-isobath PGT, which is directly related to the upwelling-linked onshore transport downstream of Point T.

Because of the uniform wind forcing used in this model, the negative PV from wind stress (Figure 10e) depends only on the water depth and is primarily offset by the positive PV from the bottom stress (Figure 10f). The bottom stress is one of the main PV-generating factors enhancing the onshore transport linked to the upwelling in the central domain. We have investigated how the PV from bottom stress balances the PV from wind stress, and have determined the effects of the interaction between along-isobath flow and topography on the upwelling process. Assuming that the bottom velocity $\boldsymbol{u_b}=\boldsymbol{U}/H$, the bottom stress is related to cross-isobath transport [*Pringle*, 2002]:

$$\boldsymbol{\tau_b}=\rho_0 r\boldsymbol{u_b}=\rho_0 r\frac{\boldsymbol{U}}{H}, \tag{6}$$

where $r\approx 2C_d|\boldsymbol{u_b}|$ based on the assumption that the contribution of bottom shear vorticity is larger than that of bottom curvature [*Liu and Gan*, 2014]. C_d is the drag coefficient. Here, r is computed from the $\boldsymbol{\tau_b}$ and $\boldsymbol{U}$ of the model outputs. The PV terms related to wind and bottom stresses (the last two terms in equation (5)) are expanded to the following [*Pringle*, 2002]:

$$\nabla\times\left(\frac{\boldsymbol{\tau_s}}{H\rho_0}\right)-\nabla\times\left(\frac{\boldsymbol{\tau_b}}{H\rho_0}\right)=\frac{\tau_s^p}{\rho_0}\frac{\partial}{\partial n}\left(\frac{1}{H}\right)-\frac{\tau_b^p}{\rho_0}\frac{\partial}{\partial n}\left(\frac{1}{H}\right)-r\frac{\bar{\xi}}{H}-\frac{1}{R}\frac{\tau_b^n}{H\rho_0}. \tag{7}$$

Since no wind stress curl in this study, the wind-driven PV is replaced by the first term on the right-hand side of equation (7). This term is a combination of the along-isobath wind stress and a coefficient accounting for shelf slope. Similarly, the PV related to both bottom stress and shelf slope (the second term on the right-hand side) is proportional to the PV term from bottom stress in PV balance. Generally, the steeper the slope, the more PV is generated, and vice versa [*Gu et al*., 2012]. The last two terms in equation (7) are related to relative vorticity and curvature vorticity. The latter is a function of the curvature radius of the isobaths, R. The cyclonically curving isobaths ($R>0$) can form an offshore transport through the forcing of bottom stress [*Gill*, 1982].

The PV balance analysis indicates that the negative JEBAR and the baroclinic bottom pressure torque terms weaken the upwelling-linked onshore transport downstream of Point T. In contrast, the onshore transport is intensified by the advection of relative and planetary PV terms. The wind stress-induced PV is balanced by the bottom stress-induced PV which is associated with process of current-topography interaction.

3.2.4. Cross-Isobath Pressure Gradient Force and Wind Stress

In addition to the primary contributors to upwelling (i.e., the along-isobath wind and pressure gradient forces), cross-isobath wind and pressure gradient forces further enhance upwelling over a shallow inner shelf [*Lü et al*., 2006; *Horwitz and Lentz*, 2014].

To diagnose the effects of cross-isobath forces on the upwelling-linked onshore transport, by utilizing equation (6), we reduce the steady and linear equations of depth-integrated motion without horizontal viscosity terms (equations (1) and (2)) to:

$$-\frac{P^n}{\rho_0}+fV^p+\frac{\tau_s^n}{\rho_0}-r\frac{U^n}{H}=0, \tag{8}$$

$$-\frac{P^p}{\rho_0}-fU^n+\frac{\tau_s^p}{\rho_0}-r\frac{V^p}{H}=0, \tag{9}$$

where $-P^n/\rho_0$ and $-P^p/\rho_0$ are the cross-isobath and along-isobath depth-integrated pressure gradient force terms, respectively. These two equations are combined to an equation of U^n:

$$U^n=\left(1+\frac{r^2}{f^2H^2}\right)^{-1}\left(-\frac{1}{f}\frac{P^p}{\rho_0}-\frac{r}{f^2H}\frac{P^n}{\rho_0}+\frac{\tau_s^p}{f\rho_0}+\frac{r}{fH}\frac{\tau_s^n}{f\rho_0}\right). \tag{10}$$

It suggests that U^n is linked to the pressure gradient force (the first term on the right-hand side) and wind stress (the third term) not only in the along-isobath direction, but also in the cross-isobath direction (the second and fourth terms). Figure 11 shows the variations in cross-isobath transport induced by these four terms along the cross-shelf section (the red line in Figure 6b).

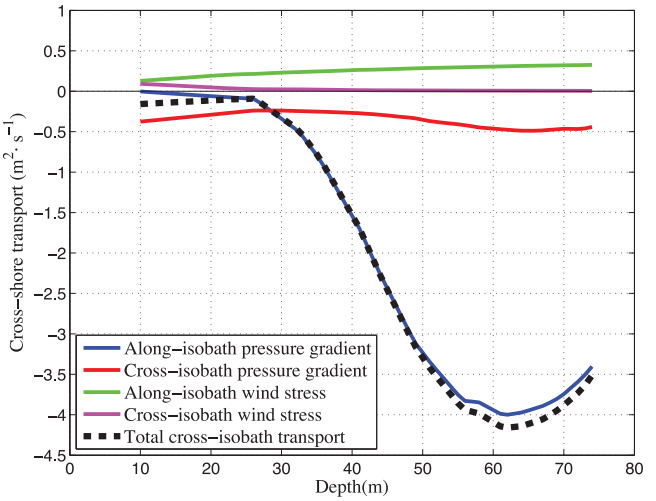

Figure 11. Cross-isobath transports, along the selected cross-shelf section shown in Figure 6b that are generated by the along-isobath pressure gradient force (blue) and wind stress (green) and the cross-isobath pressure gradient force (red) and wind stress (pink). The total transport (dashed black) is also shown. The positive (negative) values denote offshore (onshore) cross-isobath transport.

Because the averaged r ($= 2.3 \times 10^{-4}$ m s^{-1} in this study; $r = 5 \times 10^{-4}$ m s^{-1} in the study of *Pringle* [2002]) has the same order of magnitude to $f = 1 \times 10^{-4}$ s^{-1}, the coefficient $(1+r^2/f^2H^2)^{-1}$ is determined by water depth H. In the offshore area, the coefficient is close to 1, owing to the relatively large H. Thus, the first and third terms represent cross-isobath geostrophic transport and cross-isobath Ekman transport, respectively. In the offshore area (depth $>$ 30 m), the transport induced by the cross-isobath pressure gradient force approaches -0.5 m^2 s^{-1} (Figure 11). The along-isobath pressure gradient force still determines the total cross-isobath transport. It increases until it reaches its maximum amplitude at a depth of roughly 60 m. The along-isobath wind stress is crucial to offshore transport, while effect of the cross-isobath wind is negligible.

In the nearshore area (depth $<$ 30 m), instead of the along-isobath pressure gradient force, the cross-isobath pressure gradient force plays an essential role in the total transport. The geostrophic cross-isobath circulation moves the denser (lighter) water onshore (offshore) so that the cross-isobath density gradient is built up in stratified water. *Horwitz and Lentz* [2014] pointed out that the cross-shelf density gradient is critical to the cross-shelf transport over the inner shelf. In their study, an inner shelf is typically 10 m deep. As the minimum depth of the model was set to 10 m in our study, Figure 11 cannot show the conditions at depths less than 10 m. However, the cross-isobath and along-isobath wind stresses tend to be equal toward the coast. *Lentz and Fewings* [2012] noted that the cross-isobath wind stress becomes the primary force driving the cross-isobath transport over the inner shelf. The coefficient in equation (10) is small in the shallow nearshore area. The transport by cross-isobath wind stress tends to be $U^n = 0.32\tau_s^n/(f\rho_0)$, which is the empirical formula under weakly stratified conditions [*Tilburg*, 2003]. Consequently, the cross-isobath pressure gradient force is associated with the upwelling-linked onshore transport in the nearshore region. The contribution of the cross-isobath wind stress needs to be considered over the shallow nearshore shelf but could be neglected in the offshore region.

4. Discussion and Summary

Based on the correlations between upwelling-favorable wind and SST in Figure 5b, a high-correlation band has a branch extending eastward along the 75 m isobath. The SST images from satellites and models in many studies [e.g., *Jing et al*., 2011; *Li et al*., 2012] have shown that the upwelling signal frequently extends offshore to the east from the nearshore shelf off Tongluo Cape. Based on the hull-mounted ACDP measurements, *Jing et al*. [2015] showed that an eastward jet of the upwelled cold water moved away from the northeastern coast of Hainan Island. The numerical simulation in our study provides reasonable evidences that the upwelled water is offshore transported around Point T (Figure 6). The offshore transport around Point T and the onshore transport downstream show a dipole-like pattern. The offshore transport tends to be driven by the mechanisms (primarily geostrophic and Ekman balances), which is similar to those driving the onshore transport downstream (Figure 7). The offshore transport around Point T is enhanced by along-isobath PGT and wind stress, but is weakened by along-isobath PGC and bottom stress. It is worth noting that the eastward jet around Point T happens mostly in the surface layer (Figures 7 and 9). The offshore transport can also be explained by the PV balance (Figure 10). Around Point T, the offshore transport is attributed to the PV from wind stress and the advection of PV. The advection of PV is dissipated due to the current-topography interaction around Point T. In addition, the last two terms obtained from the bottom

stress-induced PV term in equation (7) reduce offshore transport around Point T where the current flows cyclonically owing to the topography.

In this study, both the observations in summer 2009 and the reanalysis data clearly present the HNEU. The probability of upwelling estimated from FCM images has two high values centers ($>$ 60%) in the regions off the eastern and northeastern coasts of Hainan Island, respectively. The upwelling off the eastern and northeastern coasts of Hainan Island is highly correlated with the wind component in 30°. To analyze the dynamics of the wind-driven upwelling process, a numerical experiment with idealized topography off the coasts of Hainan Island and Guangdong is conducted to simulate the HNEU. The corresponding onshore cross-isobath transport controls the upwelling downstream of the change in topography.

The vertically integrated momentum equations suggest that cross-isobath transport in the surface layer along the 60 m isobath has a similar distribution to that in the bottom layer, but has much smaller magnitudes. The along-isobath PGT is the primary mechanism intensifying the upwelling-linked onshore transport downstream of Point T, but the along-isobath PGC acts to retard it.

As the primary driver of the upwelling-linked onshore transport downstream of Point T, the along-isobath PGT primarily originates from the advection of relative vorticity, the gradient of momentum flux and the bottom stress curl. Furthermore, the along-isobath PGT has a dynamical balance with the along-isobath bottom PGC through variations in along-isobath surface elevation and density gradient.

On the other hand, the PGC-related baroclinic dynamics, weakening the upwelling, in the stratified water are reflected in the PV balance. The advection of planetary PV is partly balanced by the advection of relative PV. The JEBAR and the baroclinic bottom pressure torque terms dissipate the PV weakening the onshore transport downstream of Point T. The PV from wind stress is balanced by the PV from bottom stress which consists of three components related to bottom Ekman transport, relative vorticity, and curvature of bottom topography.

The study also identifies the importance of the cross-isobath force terms. The cross-isobath pressure gradient force plays an essential role in the upwelling-linked onshore transport in the nearshore regions (depth $<$ 30 m), where the contribution of the cross-isobath wind stress increases shoreward.

Our modeling study may have limitations as the flow-topography interaction is much more complicated in the real ocean than in the idealized topography used here. During summer, the SCS circulation enhances the onshore transport in the bottom boundary layer over the shelf off the eastern and northeastern coasts of Hainan Island [*Li et al*., 2012]. The bottom Ekman transport may be underestimated because the model ignores the along-shelf background current. We also omitted the effects of the freshwater flux on the nearshore area off the southern coast of Guangdong (Figure 3) and of the tides which can cause the deeper water to mix with the surface water on the continental shelf of the northern SCS.

Acknowledgments

The authors thank three anonymous reviewers for suggestions that improved this manuscript. This work was supported by the **National Basic Research Program of China** (projects **2015CB954004 and 2009CB421208**), the **National Natural Science Foundation of China** (projects **41276006 and U1405233**), and the **Hong Kong Research Grant Council** (project **16202514**). The authors acknowledge the Met Office for providing OSTIA SST data and the National Climatic Data Center for providing wind data. We also thank Zhenyu Sun, Jia Zhu, and the crew of R/V *Dongfanghong 2* for their help with collecting data which are available from the corresponding author at e-mail: hujy@xmu.edu.cn, and Laifang Li, John Hodgkiss, and Susan Sholi for help with English editing.

References

Allen, S. E. (1996), Topographically generated, subinertial flows within a finite length canyon, *J. Phys. Oceanogr.*, *26*, 1608–1632.

Austin, J. A., and S. J. Lentz (2002), The inner shelf response to wind-driven upwelling and downwelling, *J. Phys. Oceanogr.*, *32*(7), 2171–2193.

Barth, J. A., S. D. Pierce, and R. L. Smith (2000), A separating coastal upwelling jet at Cape Blanco, Oregon and its connection to the California Current System, *Deep Sea Res., Part II*, *47*, 783–810.

Chen, Z., X.-H. Yan, Y. H. Jo, L. Jiang, and Y. Jiang (2012), A study of Benguela upwelling system using different upwelling indices derived from remotely sensed data, *Cont. Shelf Res.*, *45*, 27–33.

Chen, Z. Y., X.-H. Yan, Y. W. Jiang, and L. D. Jiang (2013), Roles of shelf slope and wind on upwelling: A case study off east and west coasts of the US, *Ocean Modell.*, *69*, 136–145.

Fewings, M., S. J. Lentz, and J. Fredericks (2008), Observations of cross-shelf flow driven by cross-shelf winds on the inner continental shelf, *J. Phys. Oceanogr.*, *38*(11), 2358–2378.

Gan, J. and J. S. Allen (2002), A modeling study of shelf circulation off northern California in the region of the Coastal Ocean Dynamics Experiment, Response to relaxation of upwelling, *J. Geophys. Res.*, *107*(C9), 3123, doi:10.1029/2000JC000768.

Gan, J., J. Allen, and R. Samelson (2005), On open boundary conditions in a limited-area coastal model off Oregon. Part 2: Response to wind forcing from a regional mesoscale atmospheric model, *Ocean Modell.*, *8*, 113–115.

Gan, J., A. Cheung, X. Guo, and L. Li (2009a), Intensified upwelling over a widened shelf in the northeastern South China Sea, *J. Geophys. Res.*, *114*, C09019, doi:10.1029/2007JC004660.

Gan, J., L. Li, D. X. Wang, and X. G. Guo (2009b), Interaction of a river plume with coastal upwelling in the northeastern South China Sea, *Cont. Shelf Res.*, *29*, 728–740.

Gan, J., H. San Ho, and L. Liang, (2013), Dynamics of intensified downwelling circulation over a widened shelf in the northeastern South China Sea, *J. Phys. Oceanogr.*, *43*(1), 80–94.

Gill, A. E. (1982), *Atmosphere-Ocean Dynamics*, Academic, San Diego, Calif.

Gu, Y., J. Pan, and H. Lin (2012), Remote sensing observation and numerical modeling of an upwelling jet in Guangdong coastal water, *J. Geophys. Res.*, *117*, C08019, doi:10.1029/2012JC007922.
Guan, B. X., and S. J. Chen (1964), *Ocean Current System in East China Sea and South China Sea [in Chinese]*, Inst. of Oceanol., Chin. Acad. of Sci., Qingdao.
Han Y.W., M. B. Wang, and K. M. Ma (1990), The lowest surface water temperature area of China sea in summer: The upwelling along the east coast of Hainan Island [in Chinese], *Oceanol. Limnol. Sin.*, *21*(3), 267–275.
Horwitz, R., and S. J. Lentz (2014), Inner-shelf response to cross-shelf wind stress: The importance of the cross-shelf density gradient in an idealized numerical model and field observations, *J. Phys. Oceanogr.*, *44*(1), 86–103.
Huthnance, J. M. (1984), Slope currents and "JEBAR," *J. Phys. Oceanogr.*, *14*, 795–810.
Jing, Z. Y., Y. Q. Qi, Z. L. Hua, and H. Zhang (2009), Numerical study on the summer upwelling system in the northern continental shelf of the South China Sea, *Cont. Shelf Res.*, *29*(2), 467–478.
Jing, Z., Y. Qi, and Y. Du (2011), Upwelling in the continental shelf of northern South China Sea associated with 1997–1998 El Niño, *J. Geophys. Res.*, *116*, C02033, doi:10.1029/2010JC006598.
Jing, Z., Y. Qi, Y. Du, S. Zhang, and L. Xie (2015), Summer upwelling and thermal fronts in the northwestern South China Sea: Observational analysis of two mesoscale mapping surveys, *J. Geophys. Res. Oceans*, *120*, 1993–2006, doi:10.1002/2014JC010601.
Lentz, S. J. (2001), The influence of stratification on the wind-driven cross-shelf circulation over the north Carolina shelf, *J. Phys. Oceanogr.*, *31*(9), 2749–2760.
Lentz, S. J., and D. C. Chapman (2004), The importance of nonlinear cross-shelf momentum flux during wind-driven coastal upwelling, *J. Phys. Oceanogr.*, *34*(11), 2444–2457.
Lentz, S. J., and M. R. Fewings (2012), The wind-and wave-driven inner-shelf circulation, *Annu. Rev. Mar. Sci.*, *4*, 317–343, doi:10.1146/annurev-marine-120709-142745.
Li, L. (1990), A study on the summer upwellings in shelf waters west to Zhujiang River mouth [in Chinese], *J. Oceanogr. Taiwan*, *9*(4), 338–346.
Li, Y., S. Peng, W. Yang, and D. Wang (2012), Numerical simulation of the structure and variation of upwelling off the east coast of Hainan Island using QuikSCAT winds, *Chin. J. Oceanol. Limnol.*, *30*, 1068–1081.
Liu, Z., and J. Gan (2014), Modeling study of variable upwelling circulation in the East China Sea: Response to a coastal promontory, *J. Phys. Oceanogr.*, *44*(4), 1078–1094.
Liu, Z., and J. Gan (2015), Upwelling induced by the frictional stress curl and vertical squeezing of the vortex tube over a submerged valley in the East China Sea, *J. Geophys. Res. Oceans*, *120*, 2571–2587, doi:10.1002/2015JC010715.
Lü, X., F. Qiao, C. Xia, J. Zhu, and Y. Yuan (2006), Upwelling off Yangtze River estuary in summer, *J. Geophys. Res.*, *111*, C11S08, doi:10.1029/2005JC003250.
Mellor, G. L., and T. Yamada (1982), Development of a turbulence closure model for geophysical fluid problems, *Rev. Geophys.*, *20*, 851–875.
Mertz, G., and D. G. Wright (1992), Interpretations of the JEBAR term, *J. Phys. Oceanogr.*, *22*(3), 301–305.
Myers, P. G., A. F. Fanning, and A. J. Weaver (1996), JEBAR, bottom pressure torque, and Gulf Stream separation, *J. Phys. Oceanogr.*, *26*, 671–683.
Pringle, J. (2002), Enhancement of wind-driven upwelling and downwelling by alongshore bathymetric variability, *J. Phys. Oceanogr.*, *32*, 3101–3112.
Shchepetkin, A. F., and J. C. McWilliams (2005), Regional *Ocean Model System: A split-explicit ocean model with a free surface and topography-following vertical coordinate, Ocean Modell.*, *9*, 347–404.
Song, Y. T., D. B. Haidvogel, and S. M. Glenn (2001), Effects of topographic variability on the formation of upwelling centers off New Jersey: A theoretical model, *J. Geophys. Res.*, *106*, 9223–9240.
Song, X., Z. Lai, R. Ji, C. Chen, J. Zhang, L. Huang, J. Yin, Y. Wang, S. Lian, and X. Zhu (2012), Summertime primary production in northwest South China Sea: Interaction of coastal eddy, upwelling and biological processes, *Cont. Shelf Res.*, *48*, 110–121.
Sousa, F. M., S. Nascimento, H. Casimiro, and D. Boutov (2008), Identification of upwelling areas on sea surface temperature images using fuzzy clustering, *Remote Sens. Environ. 112*(6), 2817–2823.
Su, J., and T. Pohlmann (2009), Wind and topography influence on an upwelling system at the eastern Hainan coast, *J. Geophys. Res.*, *114*, C06017, doi:10.1029/2008JC005018.
Su, J., J. Wang, T. Pohlmann, and D. Xu (2011), The influence of meteorological variation on the upwelling system off eastern Hainan during summer 2007–2008, *Ocean Dyn.*, *61*(6), 717–730.
Tilburg, C. E. (2003), Across-shelf transport on a continental shelf: Do across-shelf winds matter?, *J. Phys. Oceanogr.*, *33*(12), 2675–2688.
Weisberg, R. H., B. D. Black, and Z. Li (2000), An upwelling case study on Florida's west coast, *J. Geophys. Res.*, *105*, 459–469.
Weisberg, R. H., Z. Li, and F. Muller-Karger (2001), West Florida shelf response to local wind forcing: April 1998, *J. Geophys. Res.*, *106*, 239–262.
Wu, R. S., and L. Li (2003), Summarization of study on upwelling system in the South China Sea (in Chinese), *J. Oceanogr. Taiwan*, *22*(2), 277–278.
Xie L. L., S. W. Zhang, and H. Zhao (2012), Overview of studies on Qiongdong upwelling, *J. Trop. Oceanogr.*, *31*(4), 35–41.
Yu W. Q. (1987), A preliminary approach of the upwelling for the northern South China Sea [in Chinese]. *Mar. Sci.*, *6*, 7–10.